Title

REACTIONS OF MODULATED MOLECULAR BEAMS WITH PYROLYTIC GRAPHITE III. OXIDATION OF THE PRISM PLANE

Authors

Olander, D.R.
Jones, R.
Schwarz, J.A.
et al.

Publication Date

1971-10-01

Submitted to Journal of
Chemical Physics

LBL-191
Preprint

REACTIONS OF MODULATED MOLECULAR BEAMS WITH PYROLYTIC GRAPHITE
III. Oxidation of the Prism Plane

D. R. Olander, R. Jones, J. A. Schwarz, and W. Siekhaus

October 1971

AEC Contract No. W-7405-eng-48

REACTIONS OF MODULATED MOLECULAR BEAMS WITH PYROLYTIC GRAPHITE

III. Oxidation of the Prism Plane

by D. R. Olander, R. Jones, J. A. Schwarz, and W. Siekhaus

Inorganic Materials Research Division of the Lawrence Berkeley Laboratory and the Department of Nuclear Engineering, University of California, Berkeley, Calif. 94720

ABSTRACT

The reaction of a modulated beam of molecular oxygen with the prism plane of pyrolytic graphite was investigated. Diffusional processes in the bulk dominated the response of the emission rates of CO and CO_2. The phase lags of these products relative to the impinging reactant beam indicated that the surface reactions were strongly affected by diffusion of oxygen in the grain boundaries then into the grains of the pyrolytic graphite structure. This double diffusion process so strongly demodulated the product signals that the apparent reactivity of the prism plane was less than that of the basal plane. This reactivity inversion is peculiar to the ac modulated beam method and would not occur in dc (steady state) experiments. The reactivity of graphite which had been annealed to 3000°C was found to be an order of magnitude larger than that of the unannealed material. This increase in reactivity was due to reduction of the demodulation effect which resulted from closing off diffusional paths in the bulk during annealing. Hysteresis of the type found in the basal plane reaction was observed in the prism plane reaction as well. Approximately one tenth as much CO_2 was produced by the reaction as CO. Reaction with a beam enriched in oxygen-18 did not show complete statistical mixing of the isotopes of oxygen in the CO_2 product. This observation suggested that a significant portion of the CO_2 product was formed by a direct reaction of surface carbon with molecular oxygen. The oxygen contained in the CO_2 product produced by this mechanism are the partners in the impinging O_2 molecule.

I. INTRODUCTION

Many studies of graphite oxidation have shown that the rate of reaction on the prism plane is greater than that on the basal plane by factors of 2.5 to 100[1]. This difference in reactivity is usually ascribed to the more chemically active nature of carbon atoms at the edges of terminated basal planes compared with atoms within the planes. The study of prism plane oxidation presented in this paper aims at explaining the mechanism of this reaction.

II. EXPERIMENTAL

Experimental techniques and data reduction methods have been presented in Part I of this series[2]. Prism plane targets were given a preliminary high temperature oxidation to remove gross surface flaws and loose chaff caused by polishing. During this preconditioning period, the reactivity decreased until it reached an equilibrium value stable over months of experimentation.

Several samples of the as-received pyrolytic graphite were used in the present experiments. All showed the same chemical behavior to within a factor of two. The bulk of the data reported here were obtained from a single specimen. A sample of the high temperature annealed graphite was also tested.

III. RESULTS

A. Surface Morphology

Fig. 1 shows the prism plane specimen used in this study. The top photomicrograph shows the surface structure after the polishing procedure described in Part I. The bottom photomicrograph shows the sample after it was retired from service. The broad band across the center is a crack which probably developed as a result of repeated thermal cycling. The structure of the reacted surface on either side

of the crack shows ridges running parallel to the basal planes (which are perpendicular to the plane of the photo). The ridges, which are ~ 5000Å apart, may represent the height that the cones attain before nucleation of new growth cones on top of old ones.

Several crevices or small pores can be seen. These may represent the "kinks" which are partially closed by high temperature annealing. Whereas the surface of the oxidized basal plane resembles a shell-torn battle field, the reacted prism plane looks like the edge of a closed book which had not been well trimmed.

B. Variation of the Apparent Reaction Probability with Surface Temperature

The variation of ε_{CO} with target temperature at two modulation frequencies is shown in Fig. 2. The apparent reaction probability is lower than that observed on the basal plane for the same temperature in the range 1100-1800°K. Whereas ε_{CO} for the basal plane passed through a maximum at about 1450°K, the apparent reaction probability on the prism plane continually increases with surface temperature. Earlier data not shown in Fig. 2 indicate that ε_{CO} continues to increase very rapidly for $T_s > 2400°K$. At $T_s = 2700°K$, a value of ε_{CO} of 0.13 was observed. There was no sign that the reaction probability was levelling off.

Previous studies have shown the prism plane reaction to be considerably faster than reaction on the basal planes.[1] The rates measured by these dc experiments are representative of the true reaction probability, whereas the modulated beam technique yields apparent reaction probabilities, which differ from the former by a frequency dependent demodulation factor. Demodulation is evident in

Fig. 2 by the factor of two separation of the data for 16 Hz and 200 Hz. We were not able to measure the dc (or zero frequency) reaction probability because the high background at mass 28 required beam modulation at least for signal-to-noise reduction. We cannot say that the true reaction probability of oxygen on the prism plane is greater than that on the basal plane at a particular temperature from the data of Fig. 2 until a reaction model which permits removal of the demodulation effect is formulated.

Fig. 2 also shows the same type of hysteresis found on the basal plane targets. The gap between the two branches is approximately the same as that found for the basal plane. The slow drift of the signal to an equilibrium value following change of surface temperature was also observed. Because of the higher temperatures attainable with prism plane samples, the hysteresis loops were closed at the high temperature end.

C. Variation of the Reaction Phase Lag with Target Temperature

The carbon monoxide phase lags obtained at the same time as the apparent reaction probabilities shown in Fig. 2 are plotted in Fig. 3. Several features of the data are noteworthy:

(1) The phase lag is essentially independent of target temperature from 1100 to 2400°K. Such behavior is most unexpected, since all reaction models based upon purely surface processes predict that the phase lag should approach zero at temperatures where the surface reaction rate constants are large compared to the chopping frequency.

(2) There is essentially no difference in the phase lag for chopping frequencies of 16 Hz and 200 Hz, which is also incompatible

with a purely surface reaction (unless the reaction involves at least four parallel branches with appropriate rate constants[3]).

(3) There is a hint of hysteresis in the phase lag measurements between 1400°K and 2000°K. The phase measured while decreasing target temperature was somewhat larger than that measured while heating up the target.

Except for target temperatures below 1100°K, we do not believe that the scatter in the points of Fig. 3 is due to the precision of the phase angle measurements. For the relatively strong signals for which the data were obtained, the phase is reproducible to within 1 or 2 degrees. The scatter in Fig. 3 is believed to be due to uncontrollable variations in the sample proper induced by changing target temperature.

D. Frequency Scan

The results of a frequency scan at a target temperature of 2100°K are shown in Figs. 4 and 5. At the lowest attainable frequency (3 Hz), the CO signal lagged the O_2 scattered signal by a bit more than 20°, and the apparent reaction probability was increasing as $\omega^{-1/4}$. We were thus never able to remove demodulation from the signal, and consequently, we could not obtain the true reaction probability even by extrapolation to $\omega = 0$.

E. Variation of the Beam Intensity

Fig. 6 shows the effect of beam intensity variations upon the CO signal amplitude. Over a 100 fold beam intensity variation, the reaction is first order in oxygen pressure. The experiments at 2300°K and 2370°K were among the first performed and show greater scatter than do the points at 2020°K. Additional experiments at

temperatures down to 1450°K (not shown on Fig. 6) also showed first order behavior. By way of comparison, the basal plane reaction was found to be first order in oxygen beam intensity for target temperatures above 1200°K.

F. Room Temperature Reaction

The reaction products CO and CO_2 were observed even when both the solid and the gas were at room temperature (300°K). In all cases except one, the product signals from this "room temperature reaction" were barely detectable ($\varepsilon_{CO} \sim 10^{-5}$). The reason that the sample shown in Fig. 1 was removed from the vacuum system was because of an abnormally large apparent reaction probability at room temperature. Just prior to removal, it exhibited $\varepsilon_{CO} \sim 10^{-3}$ at $T_s = 300°K$. The following observations were made in order to clarify the character of this signal:

(1) The signal had a definite phase relationship to the reflected O_2 signal. It lagged by 10 - 20°. By contrast, when scattered from the target, impurities in the beam such as the 4 ppm krypton, exhibited no phase lag except that due to transit and complex impedance (see Eq. (7) Part I). Noise in the instrument bears no phase relationship to the O_2 signal. In any case, the signal associated with the reaction probability of 10^{-3} was far larger than the noise.

(2) The impurities in the primary molecular beam at masses 28 and 44 were measured with the mass spectrometer located on the beam axis (see Fig. 2 of Part I). These masses represented less than 5×10^{-5} of the beam signal, and exhibited the expected transit phase lag only.

(3) The graphite specimen was replaced by a quartz disk of the same

dimensions; no CO or CO_2 reaction product was found in the beam scattered from this target. Only the small quantity of mass 28 and 44 impurities in phase with the O_2 were observed.

We believe that the signals measured at room temperature represent a true chemical reaction - that is, continuous production of CO and CO_2 from a room temperature target bombarded with oxygen. The abnormally large room temperature reactivity of the aforementioned sample at the end of its lifetime is believed to be due to accumulation of tungsten on the surface exposed to the molecular beam. Tungsten is deposited in visible amounts on the rear face of the target by evaporation from the filament of the electron beam heater. Surface migration of metals on pyrolytic graphite has been found to be rather easy[4], so that tungsten transport from the rear to the front of the sample is quite possible. In addition, opening of the crack in the sample (Fig. 1) undoubtedly facilitated tungsten contamination of the front face.

The front face of the target which showed the high room temperature reactivity was scraped to obtain a 1 mg sample for neutron activation analysis. This analysis showed 10 ppm of tungsten which is considerably higher than that of the fresh specimens (~ 10 ppb). When the scraped specimen was reinserted into the vacuum system, the reaction probability was found to be "normal" (i.e., a room temperature reaction probability of ~ 10^{-5}).

If a reaction probability of 10^{-3} were to persist in an ordinary atmospheric environment, a one inch cube of graphite would be consumed in less than 1/2 hour. Of course, surface conditions in the high vacuum of the experimental apparatus are vastly different from those

in the atmosphere, where the pressure is 10^{11} times larger. In the ordinary atmosphere outside of the vacuum chamber, the surface of the graphite is protected from oxidation by layers of adsorbed gases and other atmospheric impurities. These protective coatings are removed by heating the graphite to high temperatures and surface cleanliness is maintained by the high vacuum environment of the experimental apparatus. Nevertheless, these results suggest that substances which are assumed to be rather stable in an ordinary atmospheric environment may in fact be quite reactive in an "ultraclean" condition.

IV. REACTION MECHANISM FOR CO PRODUCTION

Except for the presence of hysteresis on temperature cycling and the fact that CO and CO_2 were the reaction products, the basal and prism planes of pyrolytic graphite behave in very different ways. The information which is most suggestive of a mechanism for CO production on the prism plane is the phase lag data of Figs. 3 and 4. The phase lag was found to be independent of (1) surface temperature over a 1300°K range, (2) beam pressure, and (3) modulation frequency up to about 200 Hz. Such behavior suggests that processes other than surface reaction are involved.

A. The Double-Diffusion Model

The solution-diffusion process discussed in Part I[2] exhibits regions in which the phase lag is independent of frequency and temperature. However, the constant phase lag for this process is 45°, whereas the phase lags of Figs. 3 and 4 are between 20 and 30°. In order to explain a temperature and frequency independent phase lag of this order, two back-to-back diffusional processes are required.

Coupled diffusion systems are encountered in materials where both grain boundary and lattice diffusion influence penetration of solute into the medium. Wolfe et al[4] have shown that metal diffusion into pyrolytic graphite proceeds via the grain boundaries (the boundaries of the growth cones) and thence by the subgrains, or small angle tilt boundaries within the grains. They found that diffusion was highly anisotropic; diffusion coefficients in the direction parallel to the basal planes were 2 to 3 orders of magnitude greater than that perpendicular to the basal planes. Thus, although bulk diffusional effects may not have been important in the basal plane study of Part II, the very much larger diffusion coefficients in the prism plane orientation makes diffusional limitations to the surface reaction a distinct possibility. The reaction is modeled as follows:

(1) O_2 chemisorbs upon surface sites with a sticking probability η_o. Since the temperature range of the prism plane measurements extended much higher than in the basal plane measurements, reduction of the sticking probability by coverage of bound CO is neglected. This assumption is substantiated by the first order dependence of the CO signal upon beam intensity at all temperatures studied. The bare surface sticking coefficient may vary with surface temperature due to the mechanisms which are responsible for hysteresis.

(2) Dissociation of molecular oxygen produces two adsorbed oxygen atoms, which is removed by two competing processes. One process

leads to bound CO which instantaneously desorbs. The other process is solution in the grain boundaries and subsequent diffusion into the bulk.

(3) The rate of the reaction step which ultimately leads to CO is taken to be proportional to the surface concentration of adsorbed oxygen. The rate constant for this step is denoted by k. We are not able to determine whether this step is controlled by a surface migration process (as was found for the basal plane[5]) or by a surface chemical reaction.

(4) The oxygen migration in the grain boundaries acts as the feed to the diffusional processes within the grains. Wolfe et al[4] consider three processes by which metal atoms penetrate the grains of pyrolytic graphite: (a) lattice diffusion by a vacancy mechanism, which they rejected because the formation energy of vacancies in graphite is greater than the activation energy of solute diffusion; (b) interstitial diffusion between basal planes of the structure; and (c) diffusion along subgrain boundaries. They rejected interstitial diffusion of metal atoms because of the high interaction energy and the insolubility of the metals in graphite. However, oxygen is a considerably smaller species than the metals they investigated and may be able to diffuse interstitially in graphite. Moreover, we have found that pyrolytic graphite which had been outgassed in vacuum above 1000°C gains considerable weight when stored in dry air for several days. Oxygen (and perhaps nitrogen as well) apparently penetrates the material quite readily, either by interstitial diffusion or diffusion along subgrain boundaries.

The overall reaction described by (1) - (4) above may be written

as:

$$O_2(g) \xrightarrow{\eta_o} 2O_{ads} \xrightarrow{k} CO(g) \qquad (1)$$

$$O_{ads} \rightleftarrows O_{gb} \rightleftarrows O_g$$

Where O_{ads} denotes atomic oxygen adsorbed on the surface, and O_{gb} and O_g denote oxygen in the grain boundaries and in the grains, respectively. The double diffusion process in the bulk is depicted schematically in Fig. 7. The grain boundaries are represented by semi infinite slabs of thickness δ which are perpendicular to the surface. The spacing between slabs is denoted by L.

Migration along grain boundaries is governed by the diffusion equation[6]

$$\frac{\partial C_1}{\partial t} = D_1 \frac{\partial^2 C_1}{\partial y^2} + \frac{2D_2}{\delta}\left(\frac{\partial C_2}{\partial x}\right)_{x=0} \qquad (2)$$

where D_1 is the diffusion coefficient of oxygen in the grain boundary and $C_1(y, t)$ is the concentration of oxygen in the grain boundaries. $C_2(x,y,t)$ is the oxygen content at a distance x within a grain, as measured from the nearest grain boundary. The point in the grain boundary from which x is reckoned is a distance y from the surface. The last term on the right of Eq. (2) represents the loss of oxygen from the grain boundary by diffusion into the grains.

The surface concentration of adsorbed oxygen is related to the concentration in the grain boundary just beneath the surface by the solubility H, or:

$$C_1(0,t) = Hn(t) \qquad (3)$$

where n(t) is the concentration of adsorbed oxygen, which is assumed to be uniform over the surface. The surface mass balance on adsorbed oxygen provides one boundary condition to Eq. (2).

$$\frac{dn}{dt} = \frac{1}{H}\left(\frac{\partial C_1}{\partial t}\right)_{y=0} = 2\eta_o I_o g(t) - \frac{k}{H} C_1(0,t) + \frac{\delta}{L} D_1 \left(\frac{\partial C_1}{\partial y}\right)_{y=0} \quad (4)$$

In Eq. (4), I_o is the intensity of the oxygen beam striking the surface and g(t) is the gating function of the modulated beam. The second term on the right of Eq. (4) represents the loss of adsorbed oxygen by the reaction which produces CO and the last term is the flux of oxygen into the bulk via grain boundary diffusion.

The second boundary condition to Eq. (2) is:

$$C_1(\infty,t) = 0 \quad (5)$$

Diffusion of oxygen within the grains is governed by:

$$\frac{\partial C_2}{\partial t} = D_2 \frac{\partial^2 C_2}{\partial x^2} \quad (6)$$

Lattice diffusion parallel to the grain boundary is neglected. The first boundary condition on Eq. (6) assumes that the concentration of oxygen at the internal surface of the grain is equal to that in the grain boundary at that location or:

$$C_2(0,y,t) = C_1(y,t) \quad (7)$$

To supply the second boundary condition, we assume that the grain dimensions are large compared to the depth of penetration of the concentration waves set up by the modulation, which leads to:

$$\left(\frac{\partial C_2}{\partial x}\right)_{x=\infty} = 0 \quad (8)$$

In the Appendix, these equations are solved for a periodic gating function and the reaction product vector is determined by the method outlined in Part I for a linear process. The results are:

$$\varepsilon_{CO} = \frac{2\,\eta_o}{\left|A^2+B^2\right|^{1/2}} \tag{9}$$

$$\tan \phi_{CO} = B/A \tag{10}$$

where A and B are given by:

$$A = 1 + F_A(\mathcal{D})S \tag{11}$$

$$B = R + F_B(\mathcal{D})S \tag{12}$$

The dimensionless constants which contain the physical-chemical parameters governing the process are:

$$R = \omega/k, \text{ the surface reaction parameter} \tag{13}$$

$$S = \frac{\sqrt{2}\,H\sqrt{D_1 D_2}}{Lk}, \text{ the solubility parameter} \tag{14}$$

$$\mathcal{D} = \left|\delta^2\omega/D_2\right|^{1/2}, \text{ the diffusion parameter} \tag{15}$$

The functions F_A and F_B are given by Eqs. (A-15a) and (A-15b) of the Appendix. They are plotted on Fig. 8.

B. Analysis of the Frequency Scan

Substitution of Eqs. (11) and (12) into Eq. (10) yields:

$$\tan \phi_{CO} = \frac{R + SF_B(\mathcal{D})}{1 + SF_A(\mathcal{D})} \tag{16}$$

Consider the limiting case of rapid diffusion within the grains ($\mathcal{D} < 0.1$). For this situation, Fig. 8 shows that:

$$F_A = \sqrt{\mathcal{D}}\cos(\pi/8) \tag{17}$$

$$F_B = \sqrt{\mathcal{D}}\sin(\pi/8) \tag{18}$$

If in addition, oxygen solubility in the grain boundaries is large enough to render $S\sqrt{\mathcal{D}} >> R$ and unity, Eq. (16) reduces to:

$$\phi_{CO} = \pi/8 \tag{19}$$

Thus, a phase lag of 22 1/2°, independent of all experimental conditions, is predicted when coupled solution-diffusion dominates the overall process. This phase lag is approximately what is observed in Figs. 3 and 4 for low modulation frequencies.

We note that the double diffusion mechanism is necessary to produce the constant phase lag of 22 1/2°. A single diffusion process alone is not sufficient. If diffusion in the grains is suppressed by making $\mathcal{D}$ large, Fig. 8 shows that $F_A = F_B = \mathcal{D}/2$. In the region of complete control by grain boundary diffusion ($S\mathcal{D} >> R$ and unity), Eq. (16) shows that $\phi_{CO} = 45°$, as was found for a similar single diffusion mechanism in Part I.

The limiting phase lag of 22 1/2° contains no information on the chemical or diffusional parameters of the system. However, the phase was observed to increase at chopping frequencies greater than ~ 200 Hz. This is attributed to the effect of the parameter R in Eq. (16), which is directly proportional to frequency. The frequency dependence of ϕ_{CO} may be most easily seen by referring the frequency-dependent terms to the standard frequency of 16 Hz. Thus we set

$$R = R_o(\omega/100) \tag{20}$$

where $R_o = 100/k$, and

$$\gamma = \gamma_o (\omega/100)^{1/2} \tag{21}$$

where $\gamma_o = (100\delta^2/D_2)^{1/2}$.

Substituting Eqs. (17), (18), (20) and (21) into Eq. (16) and neglecting unity in the denominator yields:

$$\tan \phi_{CO} = \alpha (\omega/100)^{3/4} + \tan (\pi/8) \tag{22}$$

where:

$$\alpha = \frac{R_o}{S\sqrt{\gamma_o}\cos(\pi/8)} \tag{23}$$

is a frequency independent constant.

The data of Fig. 4 were fit to Eq. (22), and a value of $\alpha = 0.030 \pm 0.008$ was determined. The solid line in Fig. 4 represents Eq. (22) with this value of α.

The theoretical curve falls below the measured phase lags at frequencies greater than 500 Hz. A possible source of the discrepancy is the use of the limiting forms of F_A and F_B for γ_o (Eqs. (17) and (18)). If γ_o is chosen as 0.1 and the exact forms of F_A and F_B are used, the dashed curve of Fig. 4 results. Although agreement with the high frequency points is somewhat improved, the points at intermediate frequencies are not well matched by the $\gamma_o = 0.1$ plot.

The apparent reaction probability corresponding to the reaction

phase lag of Eq. (22) may be shown to be:

$$\varepsilon_{CO} = \frac{\left[\frac{2\eta_o}{S\sqrt{\beta_o}\cos(\pi/8)}\right]}{\left(\frac{\omega}{100}\right)^{1/4}\left\{1 + \left[\alpha\left(\frac{\omega}{100}\right)^{3/4} + \tan\left(\frac{\pi}{8}\right)\right]^2\right\}^{1/2}} \qquad (24)$$

where α is given by Eq. (23).

The data of Fig. 5 were matched to Eq. (24) at 45 Hz, which yielded a value of 2.5×10^{-3} for the constant in the numerator. The resulting curve using $\alpha = 0.03$ is in good agreement with the measured apparent reaction probabilities.

The fact that the frequency dependencies of ε_{CO} and ϕ_{CO} both agree with the measurements does not provide additional insight into the reaction mechanism. The phase lag and apparent reaction probability are related by the Gibbs-Duhem-like relation which was described in Part I for linear processes. The agreement between theory and experiment in Fig. 5 merely demonstrates that the amplitude data are consistent with the phase measurements.

In terms of the diffusional parameters of the system, the value of α of Eq. (23) which was determined by fitting the phase lag data corresponds to:

$$\frac{L}{H\,\delta^{1/2}D_1^{1/2}D_2^{1/4}} = 6 \times 10^{-4}\ \text{sec}^{3/4}$$

at 2100°K. The ratio of α and the numerator of Eq. (24) is $R_o/2\eta_o = 12$, or, in terms of the kinetic parameters,

$$\eta_o k = 4\ \text{sec}^{-1}$$

The signal amplitude of Fig. 5 represents very significant

demodulation due to the double diffusion process. If we take η_o to be the reaction probability measured at the very highest temperature of this study ($\varepsilon_{CO} \cong 0.1$), then the above results yield $k \sim 40$ sec^{-1} at 2100°K. By contrast, the surface migration rate constant determined for the basal plane in Part II is $\sim 2 \times 10^4$ sec^{-1} at 2100°K. If k in the prism plane reaction mechanism represents surface migration, this process must be much more highly hindered than on the basal plane.

C. Temperature Dependence of the CO Phase Lag

The lack of temperature dependence of the CO phase lag suggests that restrictions which resulted in Eq. (19) are valid at all temperatures investigated here. These restrictions are:

$$\mathcal{O} = (\omega\delta^2/D_2)^{1/2} \lesssim 0.1$$

$$S\sqrt{\mathcal{O}} = \sqrt{2}\,\frac{H\delta^{1/2}D_1^{1/2}D_2^{1/4}\omega^{1/4}}{L\,k} \gg 1$$

Observance of the latter restriction implies that the quantity $S\sqrt{\mathcal{O}}$ is not highly activated. If it were, we would have expected it to be of order unity somewhere in the 1300°K temperature range covered by Fig. 3.

The above conditions imply that the phase lag at low frequency should be 22 1/2° for all surface temperatures, which qualitatively agrees with the data of Fig. 3. The fact that the phase lags at 16 Hz and 200 Hz were practically indistinguishable suggests that the reaction parameter is never comparable to $S\sqrt{\mathcal{O}}$ at low frequencies. If it were, a separation of the data for the two frequencies would have been observed.

The rise in the phase to ~ 30° at high and low temperatures may be due to loss of the "double diffusion" character of the process. If at low temperature, D_2 becomes small enough so that the parameter δ becomes comparable to unity, the phase lag starts to revert to single diffusion behavior (diffusion in the grain boundaries only). Conversely, at high temperature, grain boundary diffusion may become small compared to direct bulk diffusion into the grains from the surface, which is also a single diffusion process. Similar regimes of grain boundary and volume diffusion control are commonly observed in polycrystalline metals and ceramics[6].

D. Temperature Dependence of the CO Apparent Reaction Probability

The very complex variation of ε_{CO} with target temperature at constant frequency shown in Fig. 2 is attributed to three effects:

(1) Decrease in $S\sqrt{\delta_o}$ with increasing temperature, which, according to Eq. (24), produces larger apparent reaction probabilities ($S\sqrt{\delta_o}$ must still be large compared with unity to maintain the 22 1/2° phase lag).

(2) Changes in η_o due to surface healing processes of the type described in connection with the basal plane reaction of Part II. Such a process in undoubtedly occurring in the prism plane system as well, since hysteresis is evident in Fig. 2.

(3) Possible reduction in the sticking probability due to coverage of active dissociating sites by bound CO at very low temperatures (T_s < 1200°K). This region was not examined for reaction

order because of the low signal levels.

The apparent reaction probability increases moderately between 1000 and 1300°K. Between 1300°K and 2000°K, the temperature coefficient of ε_{CO} is even smaller. Thereafter, ε_{CO} increases rapidly, with no tendency to level off at the highest temperature attained (2700°K).

The lack of simple Arrhenius behavior in the apparent reaction probability is in part due to the surface healing process which was responsible for the decrease in ε_{CO} on the basal plane (Part II). Physical alterations of the bulk material which affects the grain boundary and sub grain diffusion parameters undoubtedly occurs because of temperature changes.

The separation of the two hysteresis loops of Fig. 2 is satisfactorily described by Eq. (24) with the bracketed term in the denominator approximated by $(\cos \frac{\pi}{8})^{-1}$ (because of the low modulation frequencies). The two loops are nearly exactly separated by a factor of $(200/16)^{1/4} = 1.9$, which strongly supports the double-diffusion model. The separation becomes somewhat greater than a factor of two at the very highest and the lowest temperatures, which is consistent with the transformation to a single diffusion process at either extreme. At the same time that the phase lag shifts from 22 1/2° towards 45°, the apparent reaction probability should change from a $\omega^{-1/4}$ to a $\omega^{-1/2}$ frequency dependence.

E. Annealed Graphite

The reactivity of annealed pyrolytic graphite in the basal plane orientation was much lower than that of the as-received material (Part II). The very same material cut for a prism plane reaction

surface was found to be the most reactive specimen encountered in this investigation. The apparent reaction probabilities for CO shown in Fig. 9 are an order of magnitude greater than those observed on as-received material (Fig. 2).

The phase lag of the CO product shown in Fig. 10 is also quite different from that of the as-received material (Fig. 3). Rather than remaining constant at 20 - 30°, ϕ_{CO} for the annealed specimen decreases from ~ 30° at low temperatures to ~ 10° at high temperatures.

Both the apparent reaction probability and the phase lag data support the bulk solution-diffusion model which was advanced to explain the behavior of the as-received prism plane graphite. High temperature annealing of pyrolytic graphite removes the substructure in the bulk which was responsible for easy penetration of oxygen into the as-received material. The dominant diffusional drain upon the population of surface oxygen atoms is thereby reduced and the demodulation which was a manifestation of this loss mechanism, is also rendered inoperative by annealing. Consequently, the apparent reaction probability increases and the phase lag decreases. Exactly the same effect of annealing was reported by Wolfe et al[4], who found that the diffusion coefficients perpendicular to the c direction of the annealed graphite were between three and four orders of magnitude smaller than those measured in the unannealed specimens.

It is clear that reduction of the diffusion coefficient in the grain or subgrain boundaries and/or removal of the grain boundaries by annealing permits more of the "surface" character of the reaction to be observed in the modulated molecular beam experiment. In terms

of the model presented earlier, this effect is reflected by a drastic reduction in the solubility parameter S (Eq. (14)), due either to lower values of D_1, D_2 and the grain boundary thickness δ or an increase in the average spacing of grain boundaries, L, or in a combination of all of these effects. The surface rate constant k is probably not as markedly affected by high temperature annealing as are the structural properties of the bulk material. As a result of the reduction in the parameter S, the second terms on the right of Eqs. (11) and (12) are comparable to unity and R in the annealed material, instead of dominating the quantities A and B. Therefore, the phase lag of Fig. 10 shows more of the usual $\tan \phi_{CO} = R = \omega/k$ behavior normally associated with a single surface reaction.

Because of the higher apparent reaction probability and concomitant cleaner signals, experiments could be performed more quickly and some additional features of amplitude hysteresis could be investigated. We were able to verify the symmetrical nature of the hysteresis described by Duval[7]. Increase of the target temperature results in a CO signal which is initially higher than the equilibrium value to which it slowly decays. Conversely, reduction of target temperature initially produces a low CO signal which subsequently increases with time to an equilibrium value.

Fig. 9 also shows that the hysteresis loop crosses itself at low temperatures. At $T_s \simeq 1400°K$, the reaction probability on the increasing temperature branch is greater than that found during a temperature decrease. Below 1400°K, however, ε_{CO} is greater on the temperature-decreasing branch. This behavior implies that more time was spent in the critical region between 1300 - 1500°K (where oxidation

creates active sites at a reasonable rate[5]) during the temperature decrease than during the measurements made while increasing temperature. The longer time was due to the larger number of data points accumulated during the temperature reduction branch of Fig. 9. We do not know how the hysteresis loop was closed at the very lowest temperature.

V. CO_2 PRODUCTION

A. Target Temperature and Beam Intensity Variations

Fig. 11 shows the dependence of the CO_2 apparent reaction probability upon target temperature. At $T_s \simeq 1100°K$, ε_{CO_2} is practically as large as ε_{CO}. With increasing temperature, ε_{CO_2} increase less rapidly than does ε_{CO}, and by $T_s \simeq 2400°K$, the CO_2/CO ratio in the product is ~ 0.1. No hysteresis is observed for the CO_2 product. ε_{CO_2} appears to be increasing rapidly at high temperatures, as did ε_{CO}.

Fig. 12 shows the CO_2 reaction phase lag obtained with the measurements of reaction probability. As with CO, ϕ_{CO_2} remains between 20 and 30° over a 1300°K temperature range.

Fig. 13 shows the CO_2 reaction to be first order with respect to oxygen beam intensity above 2000°K.

B. Isotope Mixing in the CO_2 Product

Additional insight into the CO_2 reaction was obtained by utilizing a reactant molecular beam consisting of about half $O^{18}O^{18}$ and half $O^{16}O^{16}$. The enriched gas was obtained from the Oak Ridge National Laboratory and contained 99.2 atom % O^{18}, 0.2 atom % O^{17} and 0.6 atom % O^{16}. This gas was bled into the inlet system through a variable leak and was mixed with the usual reactant oxygen of natural isotopic composition. The gas mixture passed through the cold trap which removed the $CO_2^{18\text{-}18}$ impurity in the heavy oxygen.

The initial composition of the gas scattered from the room temperature target is shown in Table 1. The mass 44 signal is mostly noise due to the residual background of CO_2^{16-16} in the vacuum chamber. Because of the absence of background at masses 46 and 48 (at least at the start of the experiments), the modulated signals due to $CO^{16}O^{18}$ and $CO^{18}O^{18}$ were quite clean. The signals due to these species definitely lag the oxygen signals, and are believed to be products of the room temperature reaction (See IIIF). Together, masses 46 and 48 represent a room temperature reaction probability of ~ 10^{-5}.

The isotope mixing experiment was conducted at T_s = 1450°K, where the CO_2 signals were sizeable. However, in the 3 hours required for accurate measurement of masses 44, 46, and 48 with the target hot, the $O^{18}O^{18}$ component of the mixed gas decreased by a factor of four (only a one half liter flask of the heavy oxygen was available). Consequently, the isotopic content of the reactant beam differed for each of the measurements of the carbon dioxide isotopes. The ratio of the signals at masses 32 and 36 was measured at the beginning and at the end of the experiment and the isotopic composition of the reactant gas at any intermediate time was estimated by assuming exponential decay of the $O^{18}O^{18}$ flow.

For the isotopic composition prevailing at the time of a particular measurement, the fraction of the three CO_2 isotopes was computed for the extreme cases of complete isotopic mixing upon reaction, and no isotopic mixing upon reaction. These results are shown in Table 2. The mass 46 in the "no-mixing" column comes from oxidation by $O^{16}O^{18}$ in natural oxygen.

Table 3 gives the measured signals at masses 44, 46, and 48, the total pressure in the source at the time the measurement was made and the computed fraction of O^{18} in the reactant beam at that time. The data of Table 3 were compared to theory by forming the ratios of the signals at two mass numbers and correcting for total pressure differences at the time of each measurement. For example:

$$\left(\frac{S_{46}}{S_{44}}\right)_{exp} = \left(\frac{1.12}{1.25}\right)\left(\frac{3.0}{3.7}\right) = 0.73$$

The ratio predicted if complete isotopic mixing occurred during the reaction is obtained by taking ratios of the entries in Column 3 of Table 2, each evaluated at the isotope fraction of the reactant beam at the time the particular signal was measured. Thus:

$$\left(\frac{S_{46}}{S_{48}}\right)_{mixed} = \frac{2x_{46}(1-x_{46})}{x_{48}^2} = \frac{(2)(0.47)(1-0.47)}{(0.37)^2} = 3.7 \qquad (25)$$

where x_{46} and x_{48} are the fractions of O^{18} in the reactant gas at the time the measurements at masses 46 and 48 were made. These are taken from Table 3.

Comparison of all of the data with the limiting cases of complete mixing and no mixing is shown in Fig. 14. The errors associated with the precision of the measurement of each signal are also shown. These results demonstrate that the reaction which produces CO_2 on the surface results in ratios of CO_2 isotopes which are only 10 - 20% of those which would be expected for complete isotopic mixing. However, the amount of mixed reaction product $CO^{16}O^{18}$ is definitely greater than that expected if no isotopic mixing occurred.

C. A Crude Model of the Surface Reactions Producing CO_2

The observation of rather incomplete isotopic mixing in the CO_2 reaction product is quite different from the results obtained by Walker et al[8] who investigated isotopic mixing in the oxidation of carbon. They found complete mixing in the reaction product. Our results, on the other hand, suggests that although some of the CO_2 is produced from oxygen atoms which belonged to different O_2 molecules, a significant portion of the CO_2 contains oxygen atoms which were partners in a particular O_2 molecule which had been chemisorbed from the beam. Fig. 14 suggests that 10 - 20% of the CO_2 is of the former type and 80 - 90% is produced by the "direct" reaction of undissociated O_2 molecules.

The direct fraction is produced by a reaction which is first order in oxygen beam intensity, which is in accord with the data of Fig. 13. The isotopically mixed CO_2, however, must be produced by an elementary surface reaction whose rate varies as the product of the surface concentrations of the oxygen isotopes involved (probably as reactants O_{ads} and CO_{ads}). Had this reaction been the dominant contributor to the signal, first order dependence of the CO_2 signal upon oxygen beam intensity would not have been observed.

The same type of hysteresis which is evident in ε_{CO} should also affect the isotopically mixed CO_2, which requires oxygen dissociation to be formed. However, the surface features which are conducive to the formation of CO_2 by a direct encounter need not be the same as the active sites which dissociate O_2. Fig. 11 shows that hysteresis is <u>not</u> found in the CO_2 reaction probability, which strongly suggests

that the active regions of the surface responsible for the observed CO_2 are not subject to the same slow oxidative generation and thermal healing processes which characterize the O_2 dissociating sites.

The isotopic content of the CO_2, the kinetic order and the absence of hysteresis in ε_{CO_2} all suggest that the majority of the carbon dioxide is produced by direct encounters of an oxygen molecule with the graphite surface rather than by a surface reaction between O_{ads} and CO_{ads}. However, the CO_2 phase lag of Fig. 12 exhibits the characteristic 20 - 30° temperature independent value which strongly suggests a double diffusion process. Had the previous results indicated an isotopically mixed CO_2 product, the phase lag could easily have been explained as that of the atomic oxygen undergoing bulk solution-diffusion prior to surface reaction to form CO_2. However, inasmuch as the other evidence suggests that direct CO_2 is predominant, the phase lag of Fig. 12 can only be explained by double diffusion of CO_2 in the graphite after formation on the surface.

VI. SUMMARY

Although the model which has been presented agrees with the broad trends of the data, it is by no means unique, nor does it consider all details. Although the model assumes that the active sites responsible for chemisorption of impinging O_2 are uniformly distributed over the surface, transport into the bulk is restricted to diffusion via the grain boundaries. Consequently, the migration of chemisorbed oxygen across the grain surfaces to the grain boundary mouths should be considered as a step in the overall process. Inclusion of this step would establish a higher concentration of adsorbed oxygen in the center of the grain surface than in the vicinity of the grain boundaries. In

the model, however, such a periodic variation of the concentration of O_{ads} over the surface was not considered.

The model also assumes that the species which migrates on the surface and diffuses in the bulk is atomic oxygen. However, a process in which chemisorption of O_2 formed mobile $(CO)_{ads}$ which subsequently diffused into the bulk and slowly desorbed from the surface would be formally described by the same surface mass balances as were applied for the O_{ads} surface species. We do not have sufficient information to determine the nature of the species undergoing diffusion into the bulk. However, the conclusion that double diffusion dominates the ac response of the system seems to us inescapable, irrespective of the nature of the species involved.

We have not attempted to analyze the hysteresis phenomenon as thoroughly as was done for the basal plane. Hysteresis in ε_{CO} on the prism plane is similar in many respects to the amplitude hysteresis described in Part II. The observation of phase hysteresis in the prism plane reaction suggests that this process is more complex than on the basal plane. In ref. 9 it is shown that addition of a small, fast (i.e., zero phase lag) process to the major reaction product vector of the double diffusion process can produce the type of hysteresis shown in Figs. 2 and 3.

Table 1. Composition of the mixed gas reflected from a room temperature prism plane graphite target

Mass no.	fraction of total signal	phase lag, deg.
32	0.40	0
34	2×10^{-3}	0
36	0.60	0
44	$< 6 \times 10^{-6}$	-
46	$6 \pm 2 \times 10^{-6}$	23
48	$5 \pm 2 \times 10^{-6}$	48

Table 2. Predicted fraction of various isotopes in the product CO_2

x = fraction of $O^{18}O^{18}$ in the Reactant Beam

Mass no.	Isotope	fraction of total CO_2 for: mixing	no mixing
44	$CO^{16}O^{16}$	$(1-x)^2$	$(1-x)$
46	$CO^{16}O^{18}$	$2x(1-x)$	$0.004(1-x)$
48	$CO^{18}O^{18}$	x^2	x

Table 3. Product CO_2 signals from a target at 1450°K

Mass no.	fraction of O^{18} in beam	Source pressure (torr)	Signal (microvolts)
44	0.55	4.3	4.9 ± 3.4
46	0.47	3.7	1.12 ± 0.2
48	0.37	3.0	1.25 ± 0.4

APPENDIX

Reaction Product Vector for the Double Diffusion Model

Since all processes in the double diffusion reaction model are linear, the fundamental Fourier terms of the response of the surface to the periodic molecular beam may be obtained by solving for the coefficients of the first Fourier components of the concentrations C_1 and C_2. Thus we set

$$\begin{aligned} g(t) &= \bar{g}e^{i\omega t} \\ C_1(y,t) &= \bar{C}_1(y)e^{i\omega t} \\ C_2(x,y,t) &= \bar{C}_2(x,y)e^{i\omega t} \end{aligned} \tag{A-1}$$

where $\bar{g}$ is the first Fourier coefficient of the gating function of the chopped beam. It is real. The coefficients $\bar{C}_1$ and $\bar{C}_2$, are complex since they lag behind the beam driving function. Substitution of Eqs (A-1) into Eqs. (2), (4) - (8) of the text yields the following differential equations and boundary conditions:

$$i\omega\bar{C}_1 = D_1 \frac{d^2\bar{C}_1}{dy^2} + \frac{2D_2}{\delta}\left(\frac{\partial\bar{C}_2}{\partial x}\right)_{x=0} \tag{A-2}$$

$$\left(\frac{k}{H} + \frac{i\omega}{H}\right)\bar{C}_1(0) = 2\eta_o I_o \bar{g} + \frac{\delta}{L} D_1\left(\frac{d\bar{C}_1}{dy}\right)_0 \tag{A-3}$$

$$\bar{C}_1(\infty) = 0 \tag{A-4}$$

$$i\omega\bar{C}_2 = D_2 \frac{\partial^2\bar{C}_2}{\partial x^2} \tag{A-5}$$

$$\bar{C}_2(0,y) = \bar{C}_1(y) \tag{A-6}$$

$$\left(\frac{\partial \bar{C}_2}{\partial x}\right)_{x=\infty} = 0 \tag{A-7}$$

Solution of Eqs. (A-5) - (A-7) yields:

$$\bar{C}_2(X,Y) = \bar{C}_1(Y)\exp\left[-\left(\frac{\delta^2\omega}{D_2}\right)^{1/2}\sqrt{i}\ X\right] \tag{A-8}$$

where X and Y are reduced distances defined by:

$$X = x/\delta \qquad \text{and} \qquad Y = y/\delta\sqrt{\Delta} \tag{A-9}$$

and $$\Delta = D_2/D_1 \tag{A-10}$$

Substituting Eq. (A-8) into (A-2) permits the function $\bar{C}_1(Y)$ to be determined. The desired quantity is the value of $\bar{C}_1$ at Y = 0, which is found to be:

$$\bar{C}_1(0) = \frac{2\eta_o\ I_o\ \bar{g}}{\frac{k}{H} + \frac{i\omega}{H} + \frac{D_1}{L\sqrt{\Delta}}\xi} \tag{A-11}$$

where:

$$\xi = \Delta^2\left(\frac{\delta^2\omega}{D_2}\right) i + 2\Delta^2\left(\frac{\delta^2\omega}{D_2}\right)^{1/2}\sqrt{i} \tag{A-12}$$

The reaction product vector is determined from the fundamental Fourier coefficient of the rate of CO production, or:

$$\varepsilon_{CO} e^{-i\phi_{CO}} = \frac{k\bar{n}}{I_o \bar{g}} = \frac{k\bar{C}_1(0)}{H\, I_o \bar{g}} \qquad \text{(A-13)}$$

Insertion of Eq. (A-11) into Eq. (A-3) and writing the results in terms of the dimensionless parameters of Eqs. (13) - (15) yields:

$$\varepsilon_{CO} e^{-i\phi_{CO}} = \frac{2\eta_o}{1 + Ri + S\sqrt{\sigma}\, i^{1/4} \left(1 + \frac{1}{2}\sigma\sqrt{i}\right)^{1/2}} \qquad \text{(A-14)}$$

The denominator of Eq. (A-14) may be converted to the form A + Bi by using the formulas:

$$i^n = \cos\left(\frac{n\pi}{2}\right) + i \sin\left(\frac{n\pi}{2}\right)$$

$$(1+ai)^{1/2} = \frac{1}{\sqrt{2}}\left[\left(\sqrt{1+a^2}+1\right)^{1/2} + \left(\sqrt{1+a^2}-1\right)^{1/2} i\right]$$

Upon performing the algebra, A and B are found to be of the form given by Eqs. (11) and (12) of the text, where:

$$F_A(\sigma) = 2^{1/4}\left[\left(\frac{\sigma}{2\sqrt{2}}\right)\left(1+\frac{\sigma}{2\sqrt{2}}\right)\right]^{1/2}\left[u \cos\left(\frac{\pi}{8}\right) - v \sin\left(\frac{\pi}{8}\right)\right] \qquad \text{(A-15a)}$$

$$F_B(\sigma) = 2^{1/4}\left[\left(\frac{\sigma}{2\sqrt{2}}\right)\left(1+\frac{\sigma}{2\sqrt{2}}\right)\right]^{1/2}\left[u \sin\left(\frac{\pi}{8}\right) + v \cos\left(\frac{\pi}{8}\right)\right] \qquad \text{(A-15b)}$$

and

$$u = \left(\sqrt{1+w^2}+1\right)^{1/2} \quad \text{and} \quad v = \left(\sqrt{1+w^2}-1\right)^{1/2} \qquad \text{(A-16)}$$

$$w = \left(\frac{\sigma}{2\sqrt{2}}\right) \Big/ \left(1+\frac{\sigma}{2\sqrt{2}}\right) \qquad \text{(A-17)}$$

The functions $F_A(\mathcal{D})$ and $F_B(\mathcal{D})$ are plotted in Fig. 8. The apparent reaction probability and the reaction phase lag for the double diffusion model are given by Eqs. (9) and (10) in the text.

LITERATURE CITED

1. A. R. Patel and O. P. Bahl, J. Nuc. Mater. 22, 226 (1967); this paper contains references to earlier work on the anisotropy in the oxidation of graphite.

2. R. Jones, D. R. Olander, W. Siekhaus and J. A. Schwarz, Part I of this series.

3. R. H. Jones, PhD thesis, AEC Report LBL-104 (1971).

4. J. R. Wolfe, D. R. McKenzie and R. J. Borg, J. Appl. Phys. 36, 1906 (1965).

5. D. R. Olander, W. Siekhaus, R. Jones and J. A. Schwarz, Part II of this series.

6. P. G. Shewmon, DIFFUSION IN SOLIDS, McGraw-Hill, pp 164-175 (1963).

7. X. Duval, Ann. Chim., Ser 12, Vol. 10, p 905 (1955).

8. P. L. Walker, Jr., F. J. Vastola, and P. J. Hart, Fundamentals of Gas-Surface Interactions, H. Saltzburg and J. N. Smith, Eds, p 307, Academic Press (1967).

9. R. H. Jones, PhD Thesis, AEC Report LBL-104 (1971).

FIGURE CAPTIONS

1. Photomicrographs of the surface of unannealed pyrolytic graphite parallel to the basal planes (i.e., the prism plane orientation): top - after polishing; bottom - after substantial oxidation by the molecular beam.

2. Variation of the CO apparent reaction probability with target temperature. Arrows on the curves through the data indicate the direction of temperature change while the data were obtained.

3. Phase lag of the CO product.

4. Frequency scan at 2100°K - phase lag.

5. Frequency scan at 2100°K - reaction probability.

6. Kinetic order of the CO signal.

7. Model for the double diffusion process.

8. Functions in the double diffusion model.

9. The CO reaction apparent probability - annealed pyrolytic graphite.

10. The CO phase lag - annealed pyrolytic graphite.

11. Apparent reaction probability of CO_2.

12. Phase lag of CO_2.

13. Kinetic order of the CO_2 reaction.

14. Isotopic mixing in the CO_2 product.

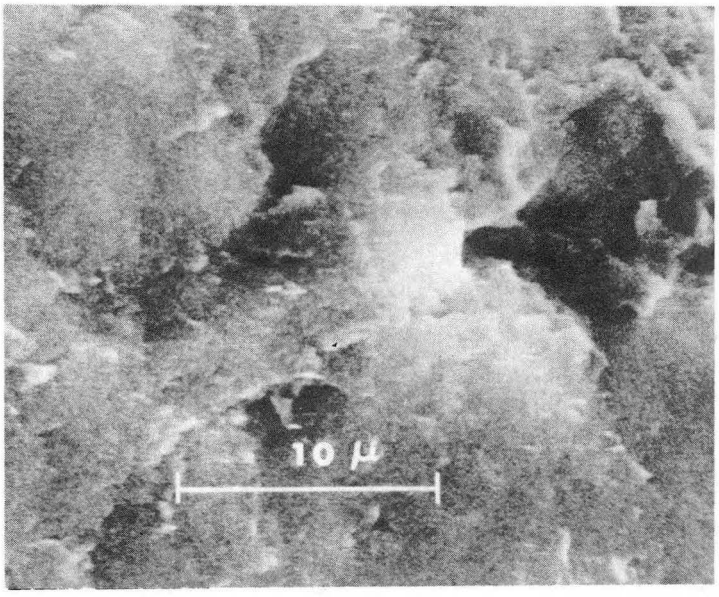

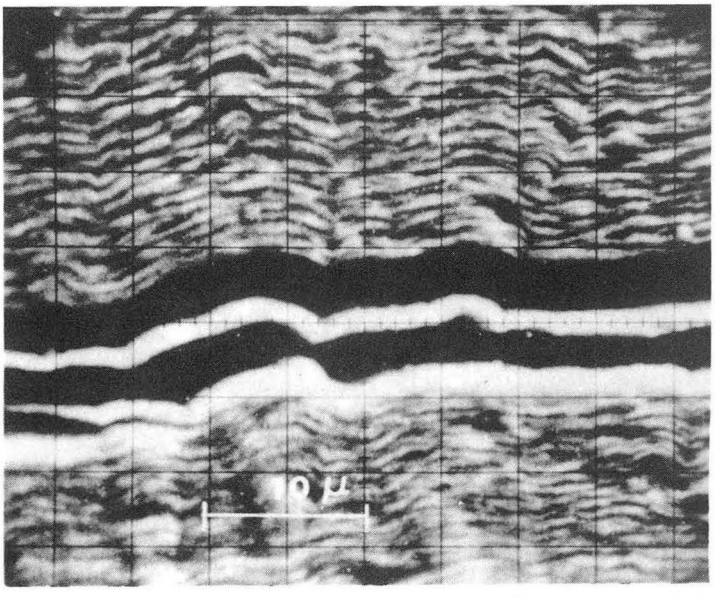

XBB 718-3770

Fig. 1

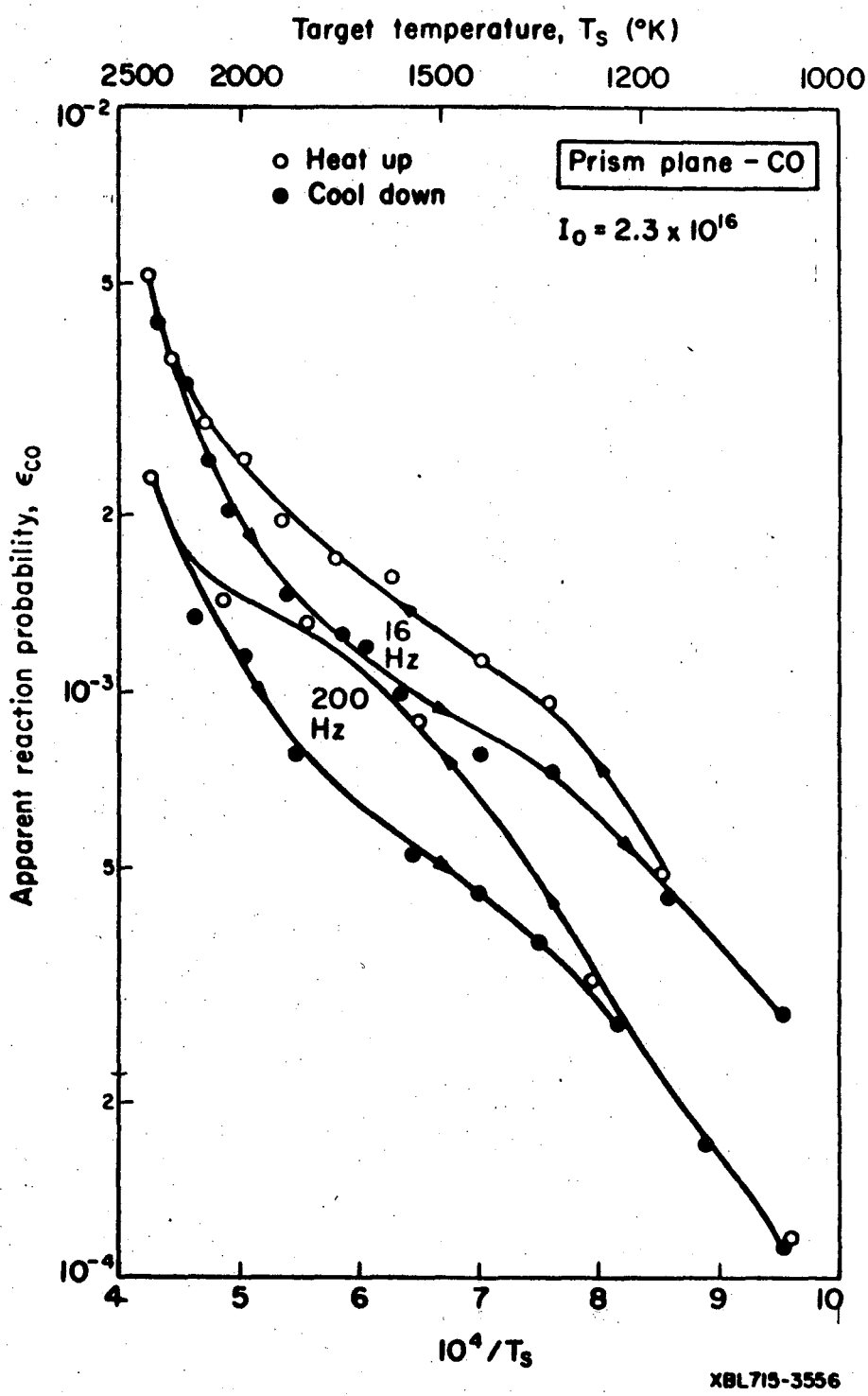
Target temperature, T_S (°K)
2500
2000
1500
1200
1000
10^{-2}
5
2
10^{-3}
5
2
10^{-4}
o Heat up
● Cool down
Prism plane - CO
$I_0 = 2.3 \times 10^{16}$
16 Hz
200 Hz
Apparent reaction probability, ϵ_{CO}
4
5
6
7
8
9
10
$10^4/T_S$
XBL715-3556

Fig. 2

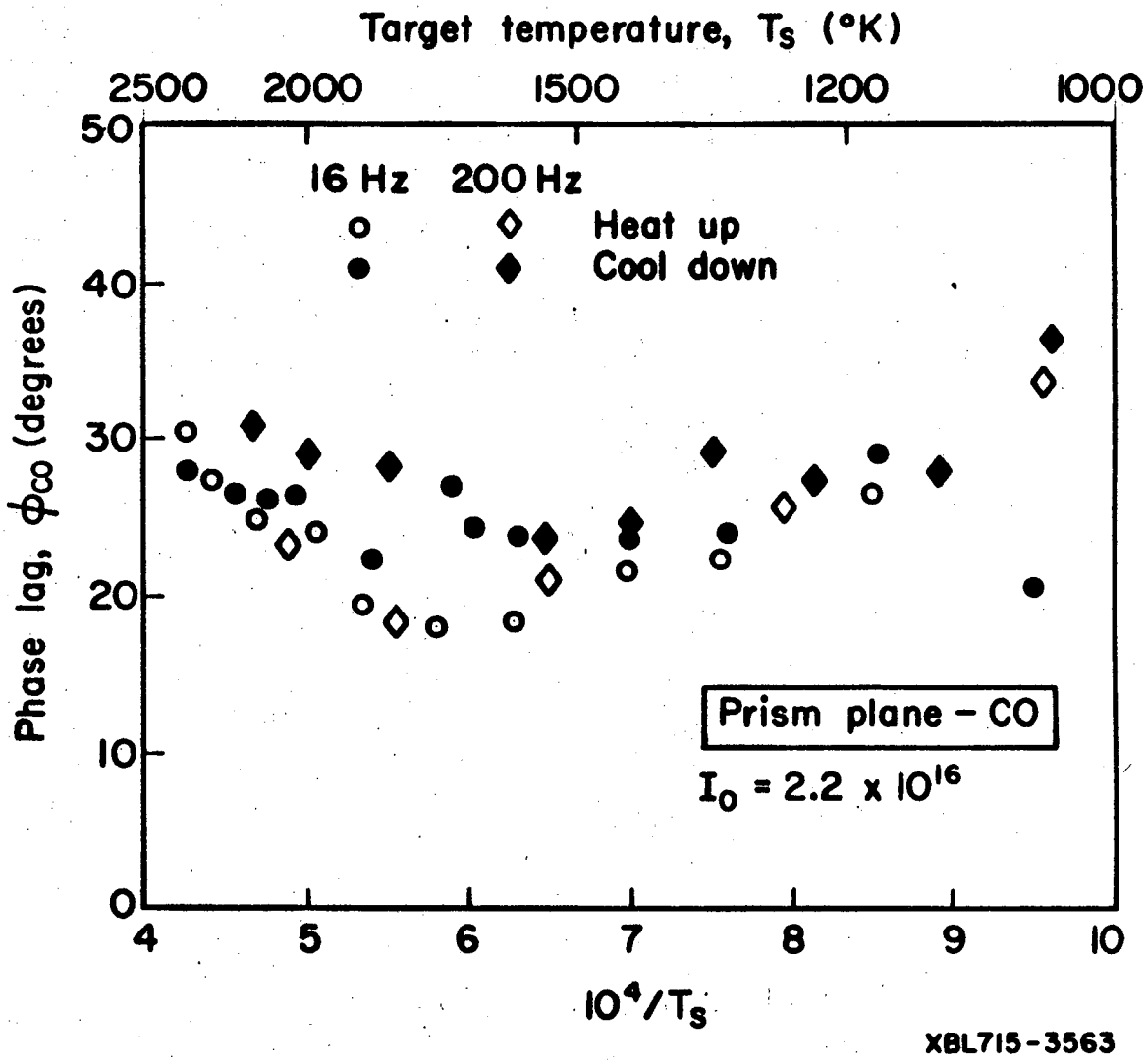
Target temperature, T_S (°K)
2500
2000
1500
1200
1000
50
40
30
20
10
0
16 Hz
200 Hz
Heat up
Cool down
Phase lag, ϕ_{CO} (degrees)
Prism plane – CO
$I_0 = 2.2 \times 10^{16}$
4
5
6
7
8
9
10
$10^4/T_S$
XBL715-3563

Fig. 3.

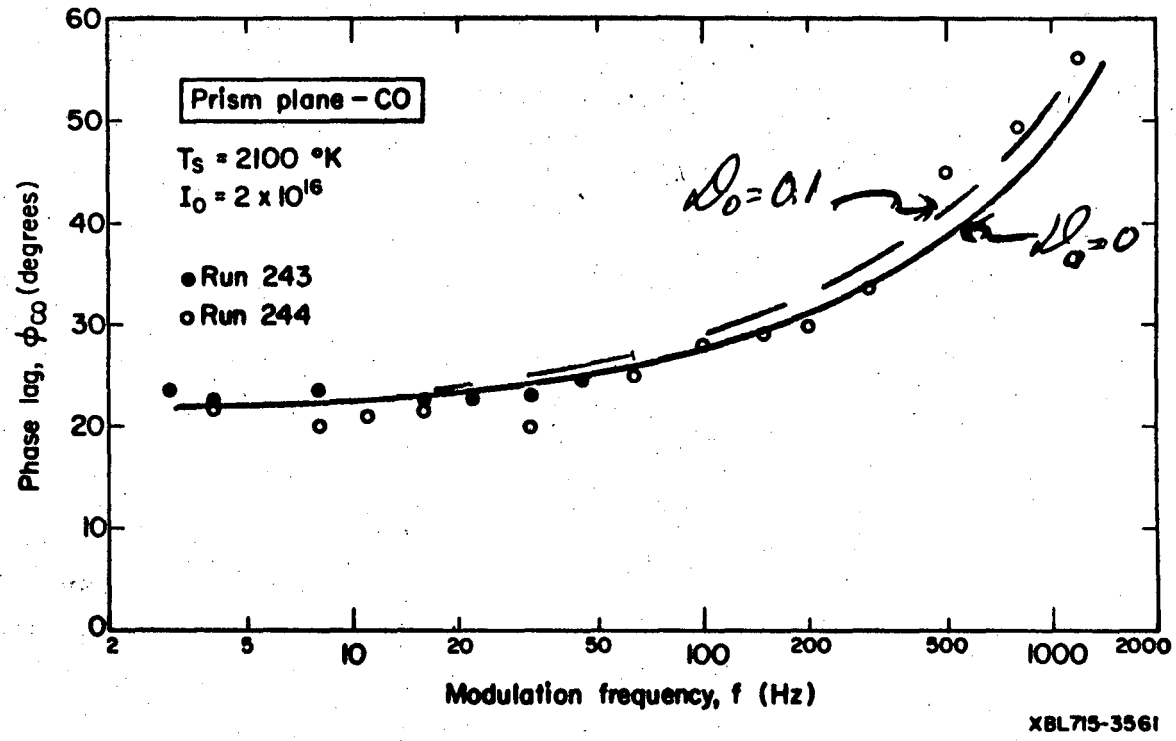
Prism plane – CO
T_S = 2100 °K
I_0 = 2 x 10^{16}
● Run 243
○ Run 244
$\alpha_0 = 0.1$
$\alpha_0 = 0$
Phase lag, ϕ_ω (degrees)
Modulation frequency, f (Hz)
0
10
20
30
40
50
60
2
5
10
20
50
100
200
500
1000
2000
XBL715-3561

Fig. 4

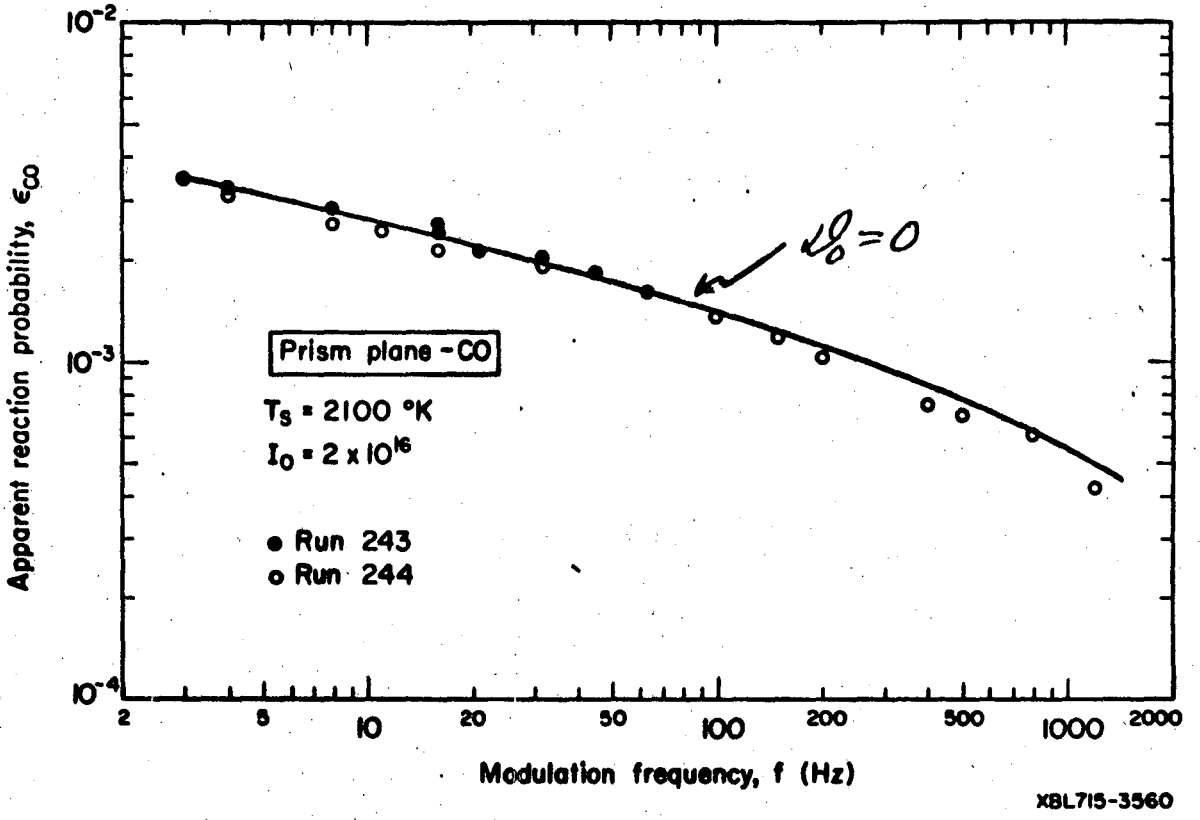
10^{-2}
10^{-3}
10^{-4}
Apparent reaction probability, ϵ_{CO}
$\alpha_0 = 0$
Prism plane - CO
T_S = 2100 °K
$I_0 = 2 \times 10^{16}$
● Run 243
○ Run 244
2
5
10
20
50
100
200
500
1000
2000
Modulation frequency, f (Hz)
XBL715-3560

Fig. 5

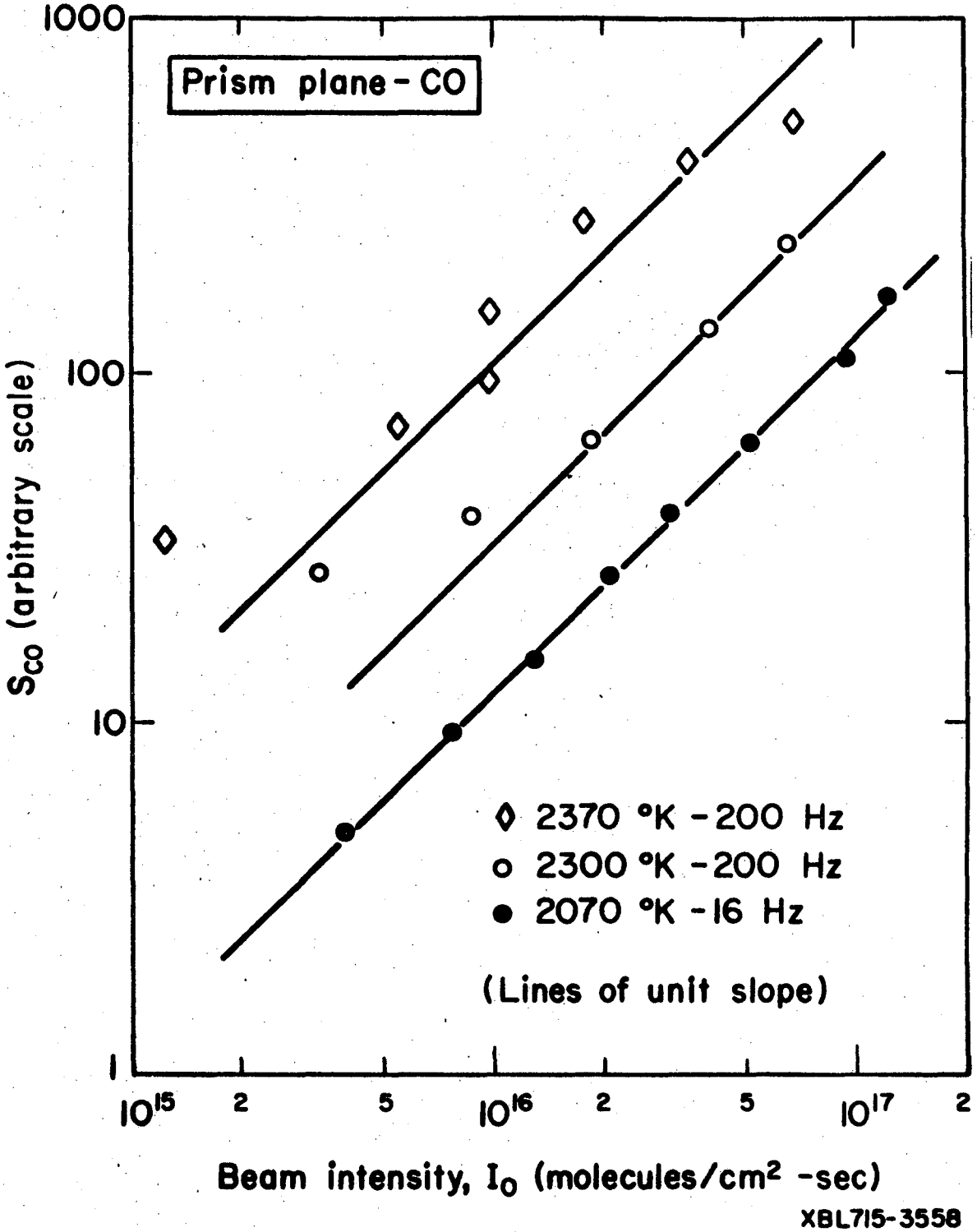
Prism plane - CO
1000
100
10
1
S_{CO} (arbitrary scale)
◊ 2370 °K - 200 Hz
o 2300 °K - 200 Hz
● 2070 °K - 16 Hz
(Lines of unit slope)
10^{15} 2 5 10^{16} 2 5 10^{17} 2
Beam intensity, I_0 (molecules/cm^2 -sec)
XBL715-3558

Fig. 6

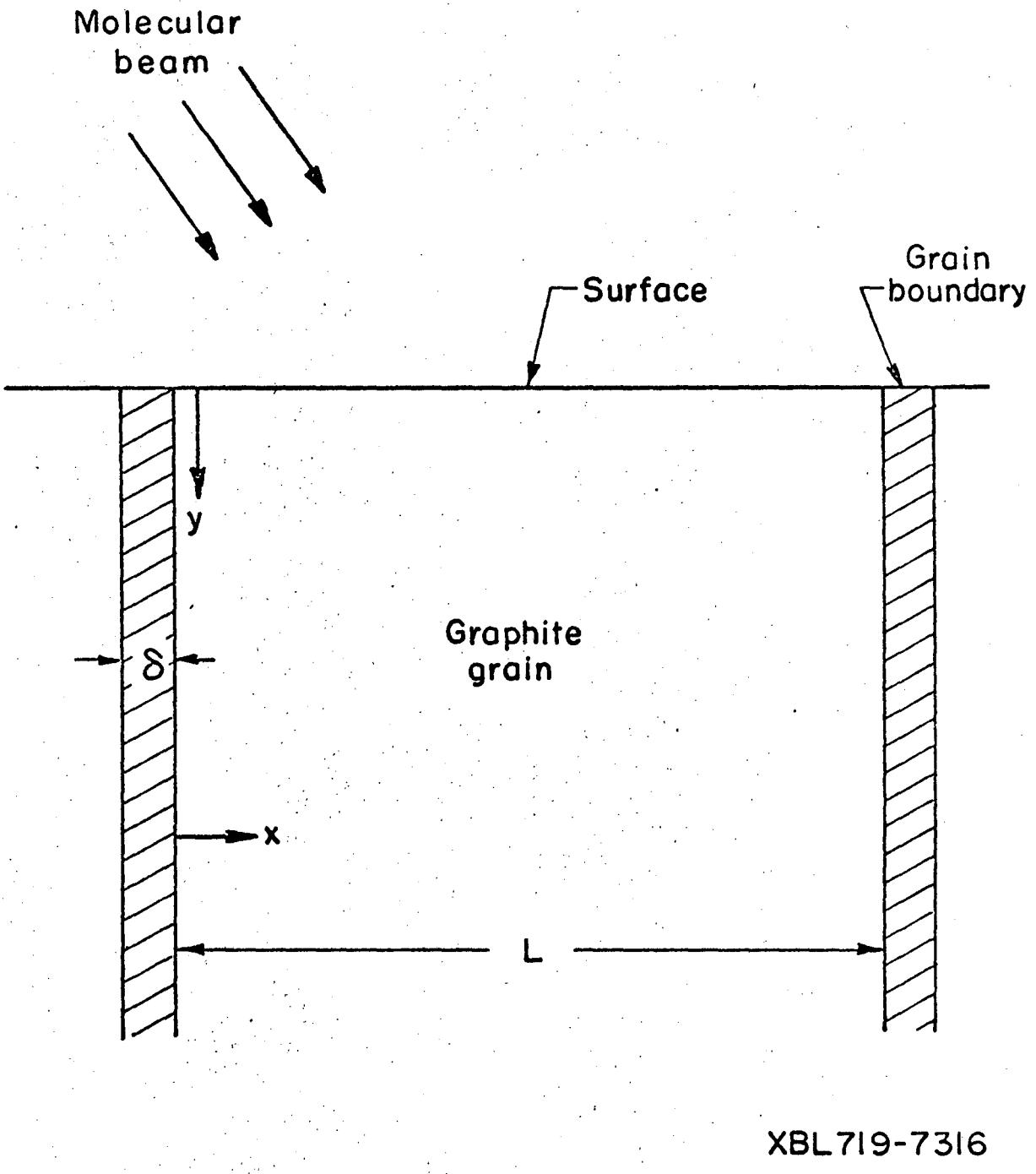
Molecular
beam
Surface
Grain
boundary
y
δ
Graphite
grain
x
L
XBL719-7316

Fig. 7

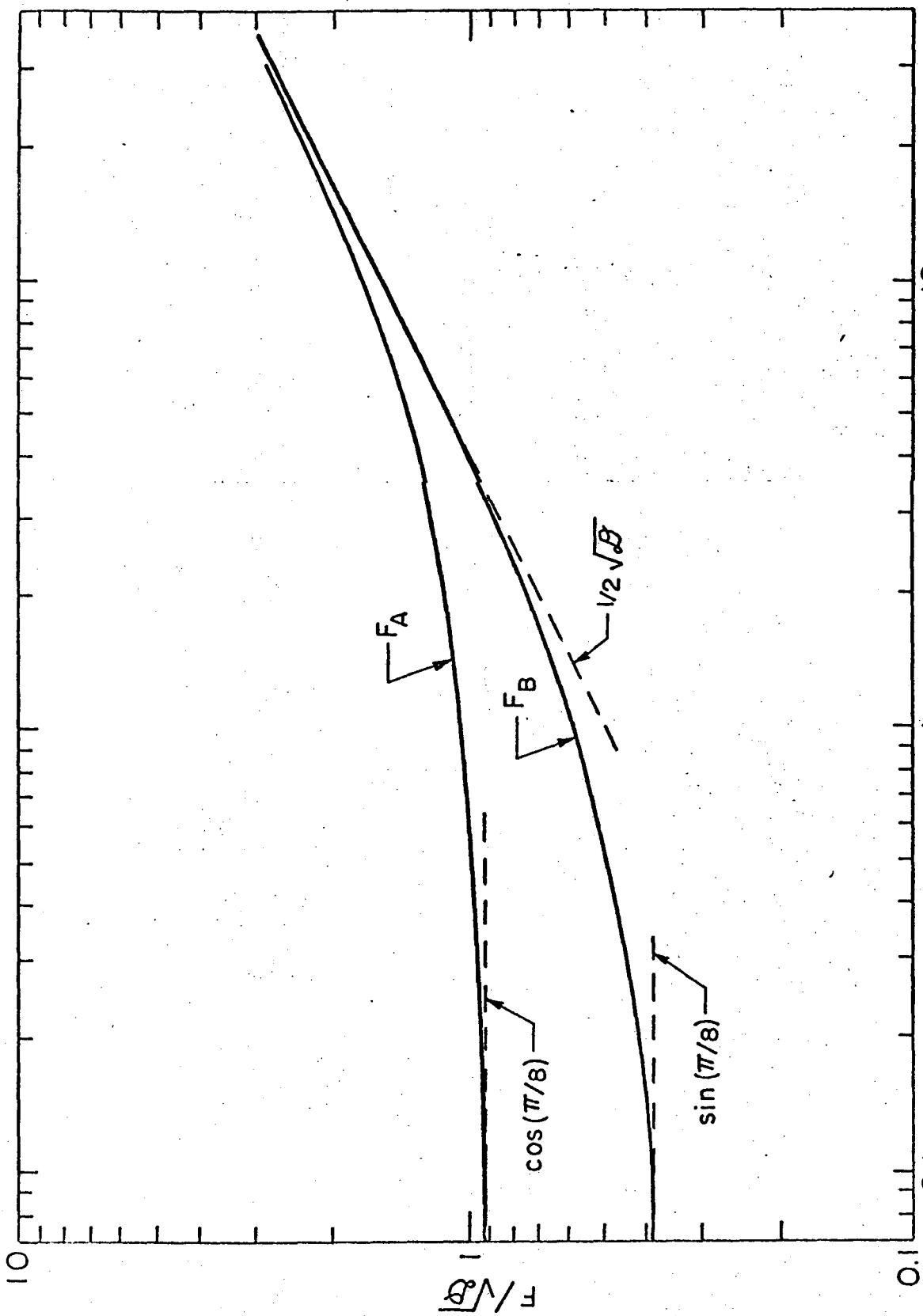

XBL719-7317

Fig. 8

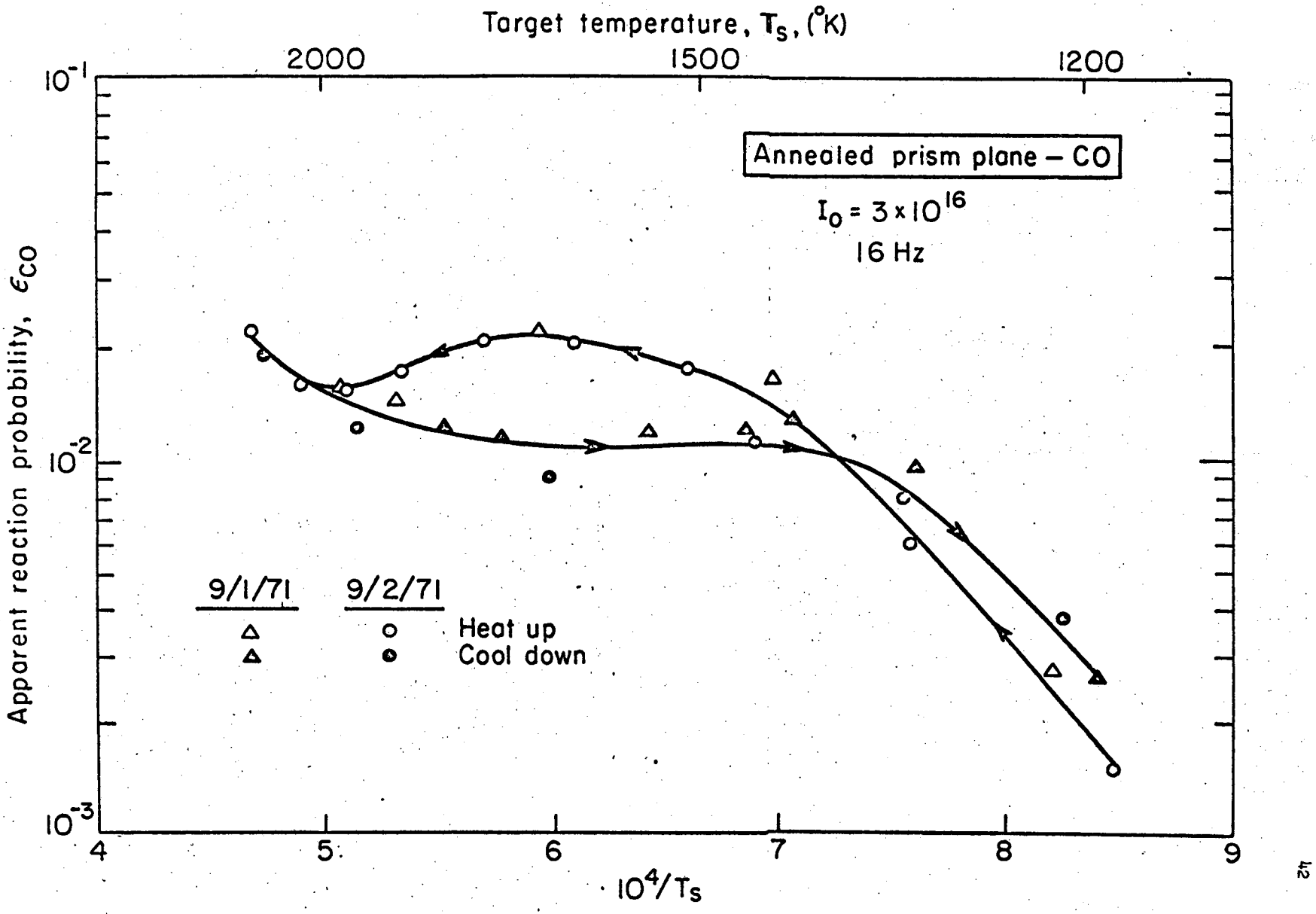

XBL 719-7322

Fig. 9

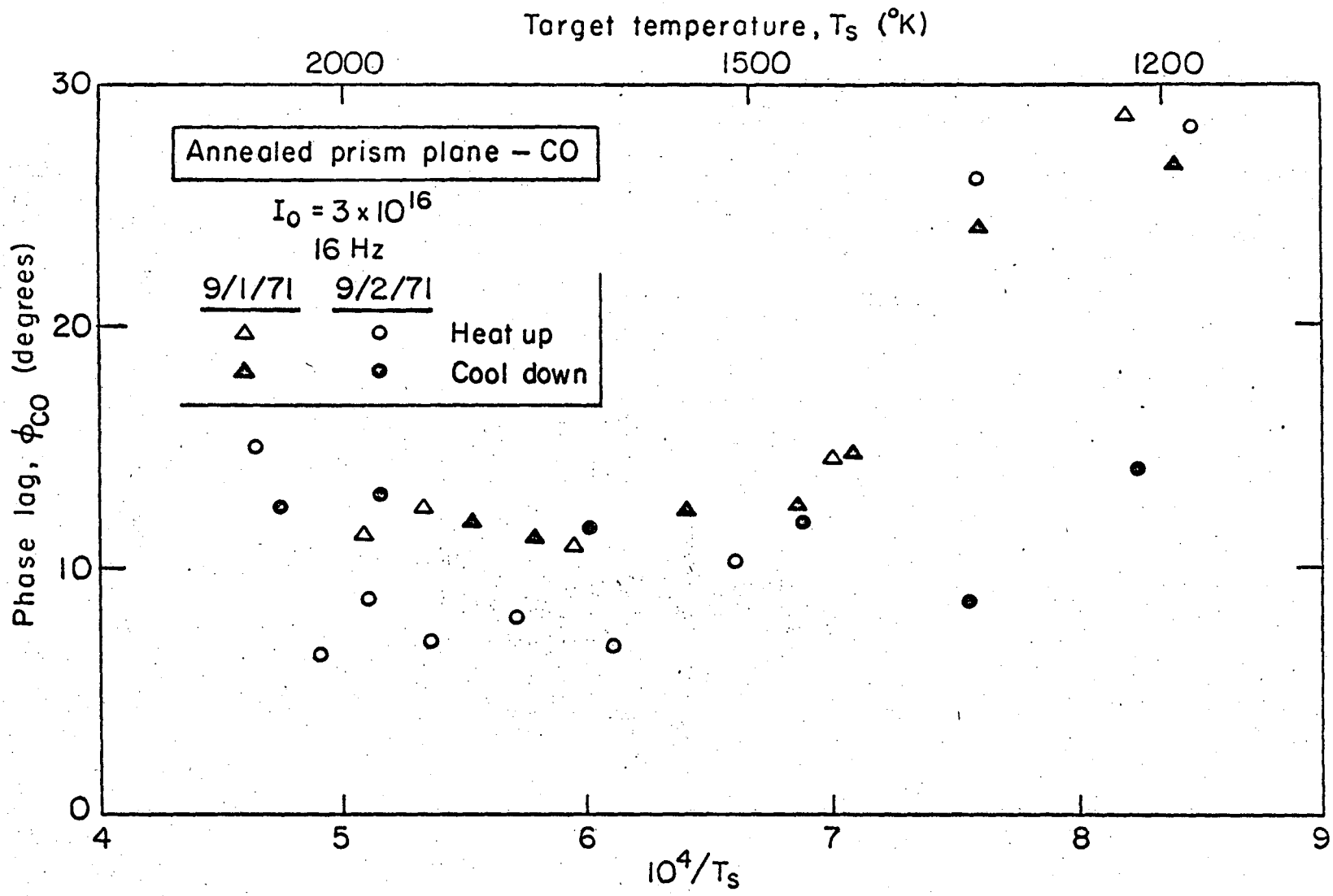
Target temperature, T_S (°K)
2000
1500
1200
Annealed prism plane – CO
$I_0 = 3 \times 10^{16}$
16 Hz
9/1/71
9/2/71
Heat up
Cool down
Phase lag, ϕ_{CO} (degrees)
30
20
10
0
4
5
6
7
8
9
$10^4/T_S$
XBL719-7321

Fig. 10

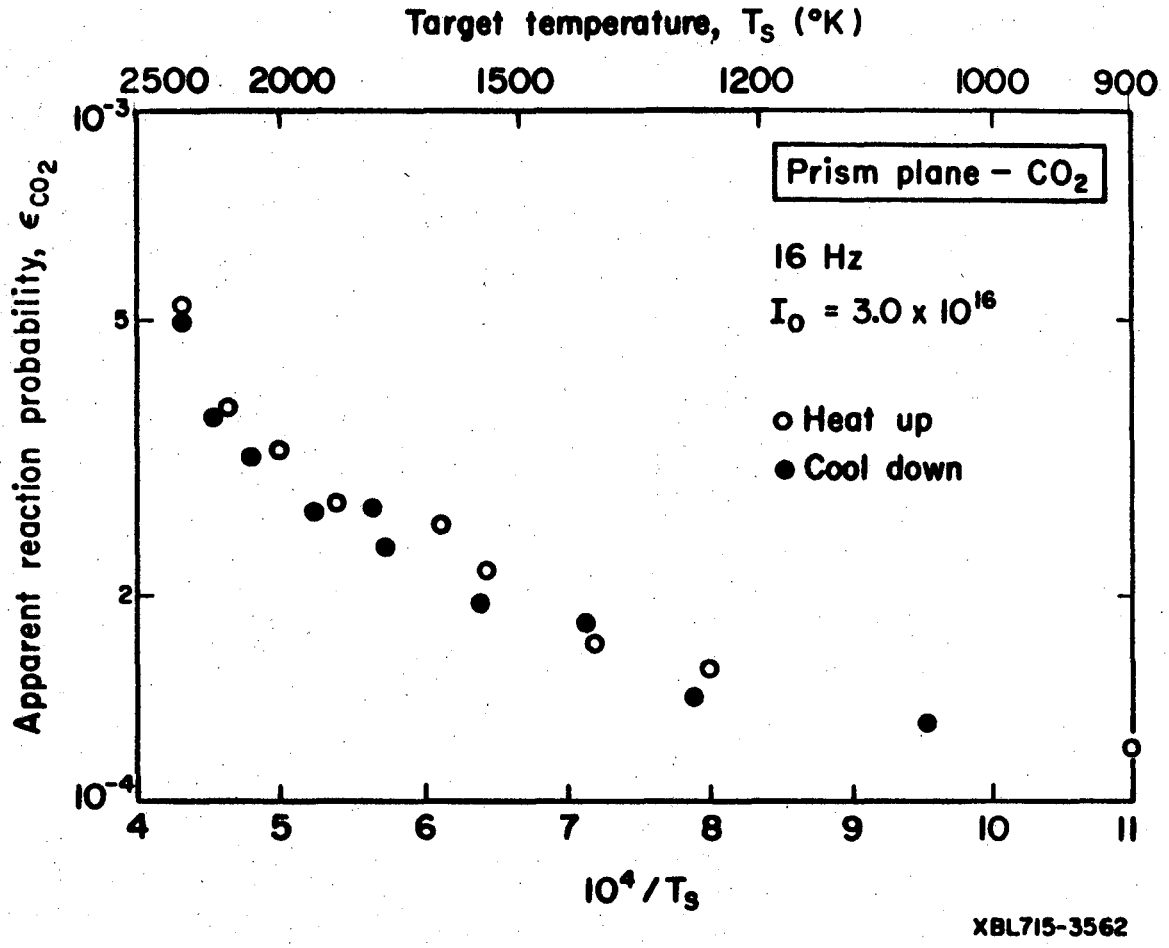
Target temperature, T_S (°K)
2500
2000
1500
1200
1000
900
10^{-3}
5
2
10^{-4}
Apparent reaction probability, ϵ_{CO_2}
Prism plane – CO_2
16 Hz
$I_0 = 3.0 \times 10^{16}$
o Heat up
● Cool down
4
5
6
7
8
9
10
11
$10^4 / T_S$
XBL715-3562

Fig. 11

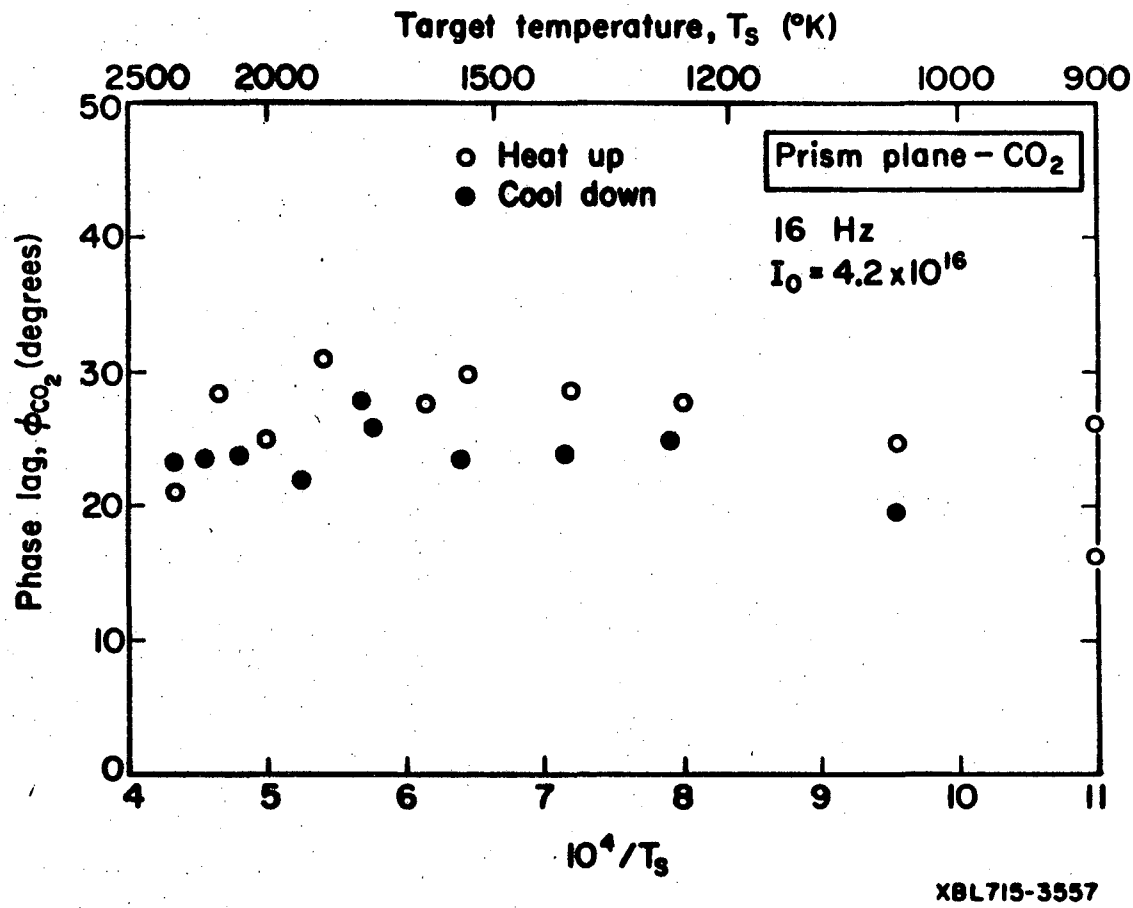
Target temperature, T_S (°K)
2500
2000
1500
1200
1000
900
50
40
30
20
10
0
Phase lag, ϕ_{CO_2} (degrees)
o Heat up
● Cool down
Prism plane – CO_2
16 Hz
$I_0 = 4.2 \times 10^{16}$
4
5
6
7
8
9
10
11
$10^4/T_S$
XBL715-3557

Fig. 12

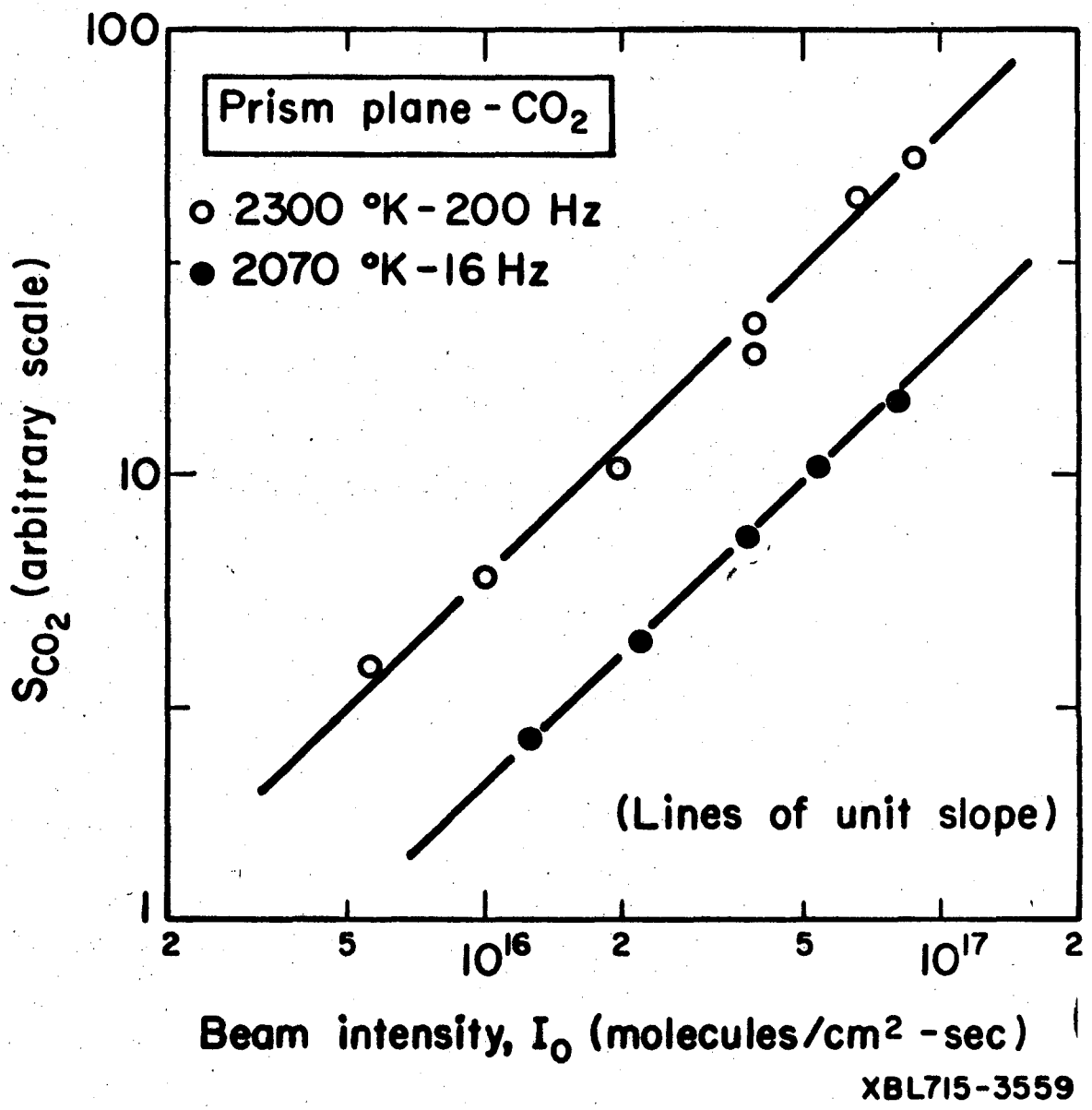
100
10
1
Prism plane - CO_2
o 2300 °K - 200 Hz
● 2070 °K - 16 Hz
(Lines of unit slope)
S_{CO_2} (arbitrary scale)
2
5
10^{16}
2
5
10^{17}
2
Beam intensity, I_0 (molecules/cm^2 - sec)
XBL715-3559

Fig. 13

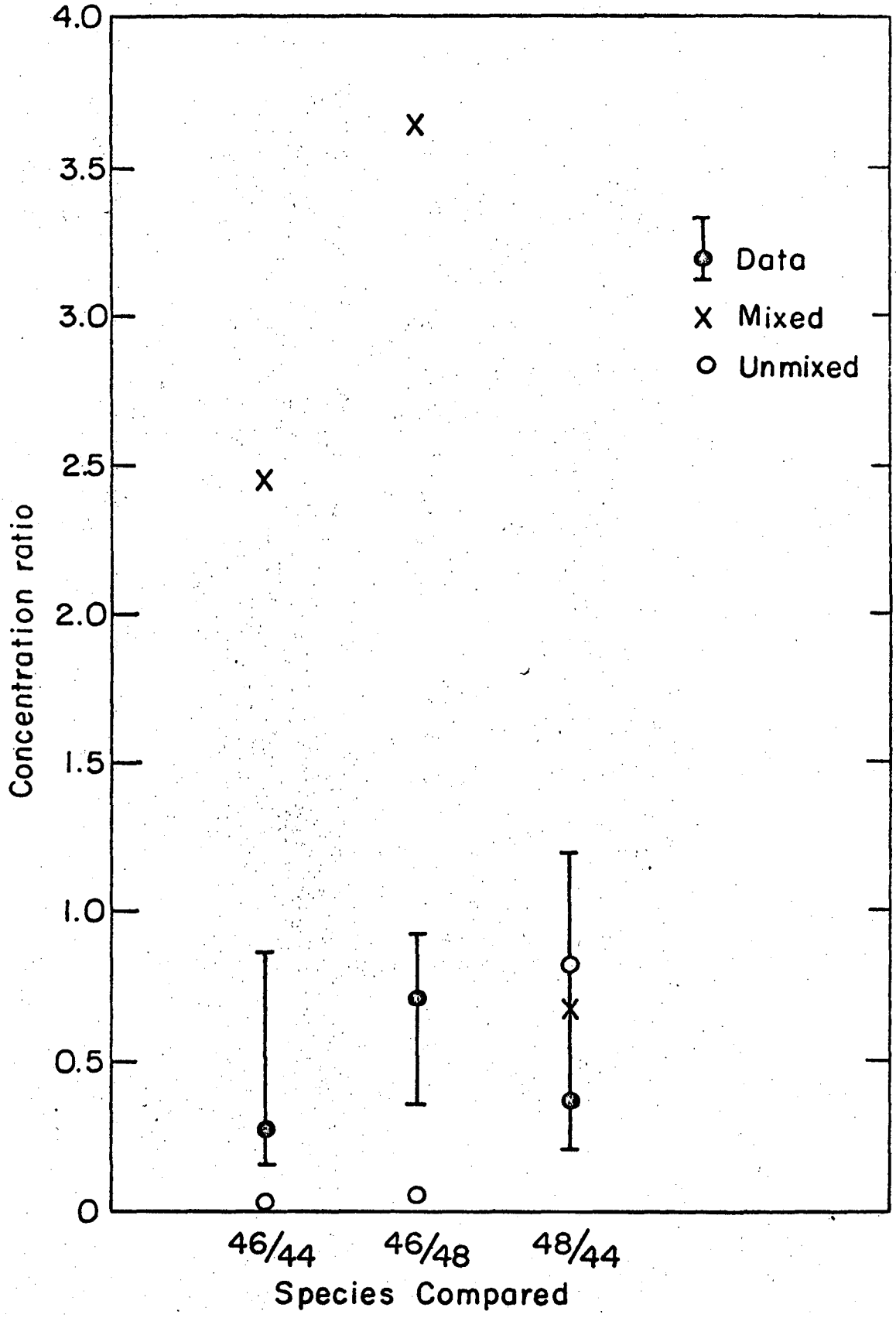

Fig. 14

XBL717-7001

TECHNICAL INFORMATION DIVISION
LAWRENCE BERKELEY LABORATORY
UNIVERSITY OF CALIFORNIA
BERKELEY, CALIFORNIA 94720